mater.scichina.com link.springer.com

Published online 13 May 2022 | https://doi.org/10.1007/s40843-021-2036-x
Sci China Mater 2022, 65(9): 2385–2392

Improving the cycling stability of lithium metal anodes using Cu_3N-modified Cu foil as a current collector

Danlei Tang, Lixia Yuan*, Yaqi Liao, Wenxuan Jin, Jie Chen, Zexiao Cheng, Xiang Li, Bin He, Zhen Li and Yunhui Huang*

ABSTRACT **Lithium (Li) metal anodes have the potential to stimulate the development of secondary batteries due to their high theoretical specific capacities and low redox potentials among all possible solid secondary anode compounds. However, the growth of Li dendrites during repeated Li stripping/plating processes leads to low coulombic efficiencies (CEs) and safety hazards, which significantly hinders their practical application. In this work, commercial Cu foil was modified *in situ* by Cu_3N nanowires (Cu_3N NWs/Cu) and used as the current collector for a Li anode. In addition to decreasing the true current density of the anode and alleviating the volume change during the cycles, Cu_3N reacted with Li during the initial cycle ($3Li + Cu_3N \rightarrow Li_3N + 3Cu$), which enabled the formation of a Li_3N-rich solid electrolyte interphase (SEI). This Li_3N-rich SEI with a high ionic conductivity not only boosted Li ion transport but also promoted the homogeneous deposition of Li *via* increased Li nucleation sites. The improvements in both mass transport and deposition dynamics restrained dendrite growth. As a result, the Cu_3N NWs/Cu anode had stable Li plating/stripping over 270 cycles with a high average CE of 98.6% at 1 mA cm^{-2}, with Li capacities of 1 mA h cm^{-2}. A long cycling lifespan of 430 cycles was achieved using a full cell with a high-load $LiFePO_4$ cathode (mass loading: 10 mg cm^{-2}) and a Cu_3N NWs/Cu–Li anode (*N*/*P* = 2.35), demonstrating the effectiveness and practicality of the Cu_3N NWs/Cu current collector in stabilizing the Li anode.**

Keywords: Cu_3N nanowires, current collectors, lithium anode, lithium metal batteries

INTRODUCTION

Lithium (Li) metal is an ideal anode for next-generation secondary batteries because of its high specific capacity (3860 mA h g^{-1}) and low redox potential (−3.040 V *vs.* a standard hydrogen electrode) [1–3] compared with other solid secondary anode compounds. However, the practical application of Li metal anodes (LMAs) suffers from Li dendrite growth, volume expansion, and severe side reactions between Li and the electrolyte [4–6]. These limitations cause low coulombic efficiencies (CEs) [7,8] and shortened cycling lifespans [9–11]. Li dendrites may also pierce the separator, causing a short circuit and thermal runaway [12,13].

To improve the rechargeability of LMAs, studies have focused on restraining the growth of Li dendrites, intensifying the solid electrolyte interphase (SEI) in the anode/electrolyte interface, and accommodating the volume expansion of the Li during the stripping/plating cycles. A wide variety of components such as poly(dimethylsiloxane) (PDMs) [14], Li polyacrylic acid [15], Li_3N [16], Li_3PO_4 [17], and Al_2O_3/poly(vinylidene fluoride-*co*-hexafluoropropylene) (PVDF-HFP) [18] have been used to construct artificial SEIs on the surface of Li anodes. Compact artificial SEIs with significantly improved chemical/electrochemical properties or mechanical strengths can prevent Li dendrite growth and suppress further side reactions. Several other electrolyte additives (e.g., $LiNO_3$ [19], Li_2S [20], $CsPF_6$ [21], $LiPF_6$ [22], and fluoroethylene carbonate [23]) can also boost the *in-situ* formation of a stable and compact SEI. During the initial electrode process, additives are easily reduced by Li and generate inorganic phases such as Li_3N and LiF, which can enhance the chemical stability and compactness of the SEI.

Although an optimized SEI can restrain dendrite growth and prevent side reactions, intrinsic volume expansion can destroy the integrity of the SEI, especially when the cells operate at high current densities and a low Li excess [24]. If the *in-situ*-formed or pre-constructed SEIs are not completely uniform, they can cause Li^+ flux at the interface, leading to the formation of Li dendrites [25,26]. Therefore, constructing an ideal matrix for Li deposition while optimizing the SEI is an effective method to improve the rechargeability of the Li anode. Cu is the most commonly used current collector for anodes [27]. Three-dimensional (3D)-structured Cu has been studied as a current collector for Li anodes as it provides a host for deposited Li and effectively homogenizes local current densities. The energy density of these cells is largely reduced due to the thickness and high mass fraction of the anode system [28,29]. Cu foils with hybrid structures modified by 3D submicron skeletons are attractive materials due to their lightweight nature. Several chemically active materials such as CuO [30], Cu_2S [31], and Cu_3P [32] have been used to modify Cu foil. The 3D submicron structure provides a skeleton for Li deposition, reducing the volume change caused by Li plating/stripping. These chemically active materials with lithiophilic elements can react with Li and

State Key Laboratory of Materials Processing and Die & Mould Technology, School of Materials Science and Engineering, Huazhong University of Science and Technology, Wuhan 430074, China
* Corresponding authors (emails: huangyh@hust.edu.cn (Huang Y); yuanlixia@hust.edu.cn (Yuan L))

solid products such as Li_2O, Li_2S, and Li_3P, provide nucleation sites for Li plating, and contribute to the formation of an SEI with greater stability.

In this work, Cu_3N nanowires (NWs) were grown on the surface of a commercial Cu film *via* simple chemical reactions. The obtained hybrid microstructure (Cu_3N NWs/Cu) acted as an ideal host for Li deposition. For the bare Cu foil, both the high nucleation barrier on the lithiophobic Cu and the uneven Li flux near the interface accelerated the growth of Li dendrites (Fig. 1a). For the Cu NWs/Cu system, the 3D NW structure uniformly affected the Li ion flow and electric field distribution. This structure suppressed dendrite growth, but the lithiophobicity of the Cu led to a disordered and loose Li deposition (Fig. 1b). In the Cu_3N NWs/Cu system, in addition to improving mass transport and lowering the true current density, the Cu_3N reacted with Li during the initial Li plating process ($3Li + Cu_3N \rightarrow Li_3N + 3Cu$), forming Li_3N-rich channels with high ionic conductivities on the Cu foil, which guided a homogeneous distribution of the Li ion flux. The lithiophilic Li_3N resulted in uniform Li nucleation, which led to dense Li deposition (Fig. 1c). Li_3N also contributed to a high-performance SEI. Li_3N has a high room-temperature ionic conductivity of 6×10^{-3} S cm^{-1} and a high Young's modulus [33]. Therefore, the Li_3N-rich SEI could bear the volume change caused by the Li plating/stripping, preventing side reactions between Li and the electrolyte by minimizing cracks in the SEI layer [34]. As a result, the Li anode with a Cu_3N NWs/Cu current collector achieved a high average CE of 98.6% for >270 cycles (1 mA cm^{-2}; 1 mA h cm^{-2}) and 98.9% for >100 cycles (1 mA cm^{-2}; 4 mA h cm^{-2}). The LiFePO$_4$|Li full cell also demonstrated a high capacity retention ratio of 90% after 430 cycles, indicating the potential of this current collector for practical applications.

EXPERIMENTAL SECTION

Fabrication of the 3D Cu_3N NWs/Cu current collector

A Cu film (10 μm) was submerged in a mixed solution of 2 mol L^{-1} NaOH and 0.1 mol L^{-1} $(NH_4)_2S_2O_8$ for 30 min to form the 3D $Cu(OH)_2$ NW structure ($Cu(OH)_2$/Cu) [35]. After rinsing with deionized water and drying in the air (70°C) for 12 h, the $Cu(OH)_2$/Cu hybrid was placed in a tube furnace and heated under an Ar gas flow with urea on the side of the Ar inlet as a nitrogen source at 180°C for 2 h. Urea was used as the nitrogen source because it decomposes into NH_3 under heating. Then, the temperature was then increased to 300°C and held for 3 h. Cu_3N NWs were synthesized by nitridation between the $Cu(OH)_2$ NWs and NH_3 at 300°C. After cooling to room temperature, a 3D Cu_3N NWs/Cu current collector was obtained.

Fabrication of the 3D Cu NWs/Cu current collector

The obtained $Cu(OH)_2$/Cu was placed in a tube furnace and heated under an Ar/H_2 gas flow at 180°C for 2 h. The temperature was then increased to 300°C and maintained for 3 h. A 3D Cu NWs/Cu current collector was then obtained. After cooling to room temperature, the 3D Cu NWs/Cu current collector was punched into disks (φ = 12 mm in diameter), and the disks were quickly transferred to an Ar-filled glove box.

Material characterization

Phase analysis was conducted by powder X-ray diffraction (XRD, Cu-Kα, Empyrean). A field emission scanning electron microscope (SEM, Quanta 650 FEG) was used to visualize the material morphologies, and an energy dispersive X-ray spectrometer was used to identify the elemental compositions. To observe the deposited Li on different matrices, the cycled cells

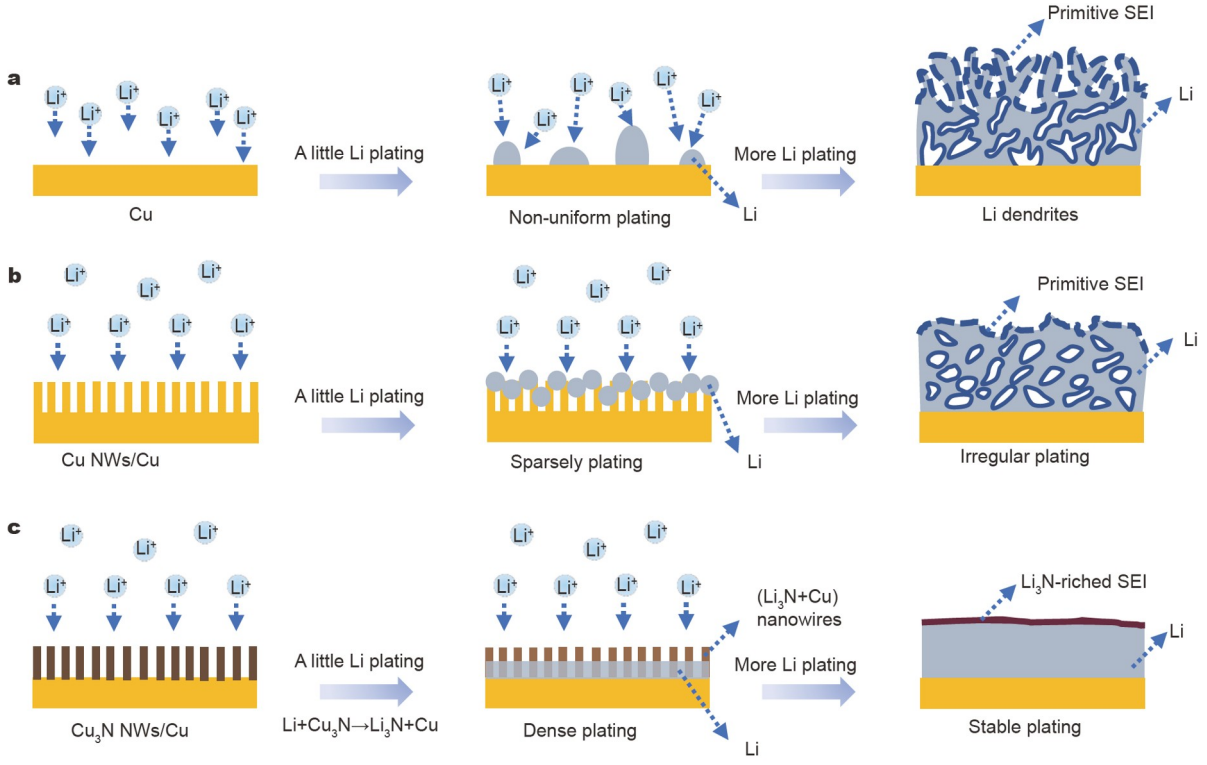

Figure 1 Schematic comparison of the Li plating behaviors on (a) Cu foil, (b) a Cu NWs/Cu current collector, and (c) a Cu_3N NWs/Cu current collector.

were disassembled in an Ar-filled glove box. The Li-deposited electrodes were then washed three times in dimethoxyethane (DME) and dried in an Ar-filled glove box at room temperature. An X-ray photoelectron spectrometer (AXIS-ULTRA DLD-600W) was used to further analyze the components of the SEI.

Electrochemical measurements

Standard CR2032 coin cells were assembled with Cu_3N NWs/Cu or Cu NWs/Cu foils (φ = 12 mm) as the working electrodes and the Li foil as the counter electrode in an Ar-filled glove box. The electrolyte was 1 mol L^{-1} lithium bis(trifluoromethanesulphonyl)imide (LiTFSI) in a mixture of 1,3-dioxolane (DOL) and DME (1:1 by volume) with 2 wt% $LiNO_3$. All cells tested contained 40 μL of the electrolyte. Cyclic voltammetry (CV) was performed using an electrochemical workstation (CHI600D). The cycling performance and CE of the half-cells (Cu_3N NWs/Cu|Li, Cu NWs/Cu|Li, and Cu|Li) were tested on a Land battery measurement system (Land, China). To test the CE, all half-cells were cycled from 0 to 1 V at 0.5 mA for three cycles to form the SEI. The cells were then tested at 1 mA cm^{-2} for different Li deposition capacities (1 and 4 mA h cm^{-2}). Electrochemical impedance spectra (EIS) were measured at the 0th, 50th, and 100th cycles (Li stripping state). The cycle stability of the Li/Li symmetric cells was tested at 1 mA cm^{-2} for the 4 mA h cm^{-2} Li deposition. For the Li/$LiFePO_4$ (LFP) full cell, the pre-lithiated matrices (Cu_3N NWs/Cu–Li, Cu NWs/Cu–Li, and Cu–Li) with 4 mA h cm^{-2} Li deposition were used as the anodes. The LFP cathode was prepared from a slurry that contained 80 wt% commercial LFP powder, 10 wt% Super P, and 10 wt% PVDF. The slurry was coated onto the carbon-coated Al foil and punched into disks (φ = 8 mm) after being dried. The mass loading was ~10 mg cm^{-2}.

RESULTS AND DISCUSSION

As shown in Fig. 2, $Cu(OH)_2$ NWs were grown *in situ* on the surface of a Cu foil precursor that was soaked in a mixed solution of NaOH (2 mol L^{-1}) and $(NH_4)_2S_2O_8$ (0.1 mol L^{-1}). The $Cu(OH)_2$/Cu was then reduced to Cu_3N *via* Ar-H_2 gas flow at 300°C (Fig. 2a). For the $Cu(OH)_2$/Cu hybrid, the original yellow Cu foil was completely covered by the blue $Cu(OH)_2$ (Fig. 2c, d). The diffraction peaks in the XRD spectrum matched the PDF#13-0420 of $Cu(OH)_2$ (Fig. 2b). The SEM image in Fig. 2h clearly shows the NW structure of $Cu(OH)_2$, with an average NW length of ~10 μm. After heat-treatment in Ar-H_2 gas, the blue $Cu(OH)_2$ transformed into brown Cu_3N (Fig. 2d, e) and corresponded with the PDF#47-1088 of Cu_3N (Fig. 2b). To protect the sample from corrosion by the decomposition products of urea, it was placed between two corundum plates during the heating process (Fig. 2a). The elemental distribution maps in Fig. 2f demonstrate the homogeneous distribution of N and Cu. Fig. S1c shows the morphology of a Cu NWs/Cu hybrid control sample, which also demonstrates a fiber structure. The thickness of the Cu NWs layer was ~10 μm, which was the same as the Cu_3N NW layer (Fig. S1d and Fig. S2).

Fig. 3 compares the morphologies of the deposited Li from

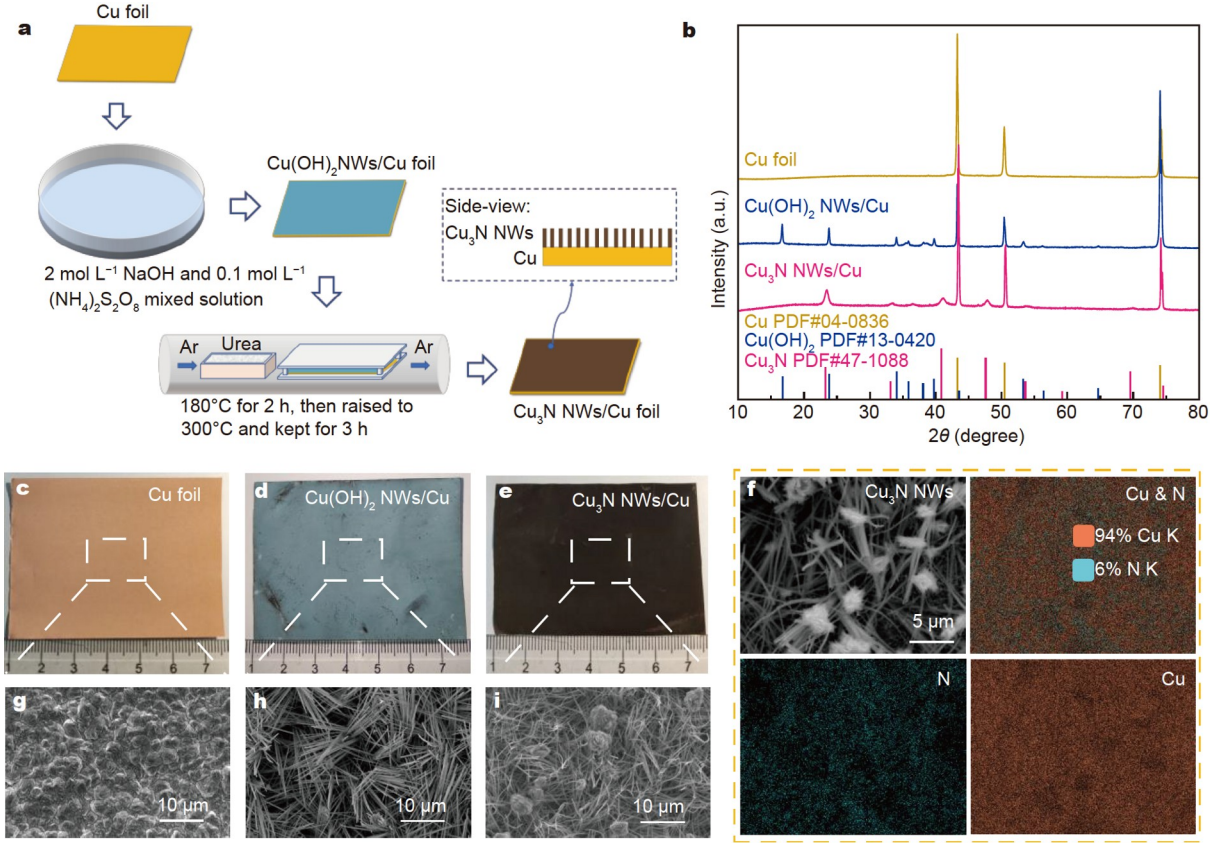

Figure 2 (a) Schematic of the preparation of the Cu_3N NWs/Cu current collector. (b) XRD patterns of the Cu foil, $Cu(OH)_2$ NWs/Cu, and Cu_3N NWs/Cu. Photographs of the (c) Cu foil, (d) $Cu(OH)_2$ NWs/Cu, and (e) Cu_3N NWs/Cu. (f) Surface SEM image of Cu_3N NWs/Cu and corresponding elemental distribution maps. The surface morphologies of the (g) Cu foil, (h) $Cu(OH)_2$ NWs/Cu, and (i) Cu_3N NWs/Cu.

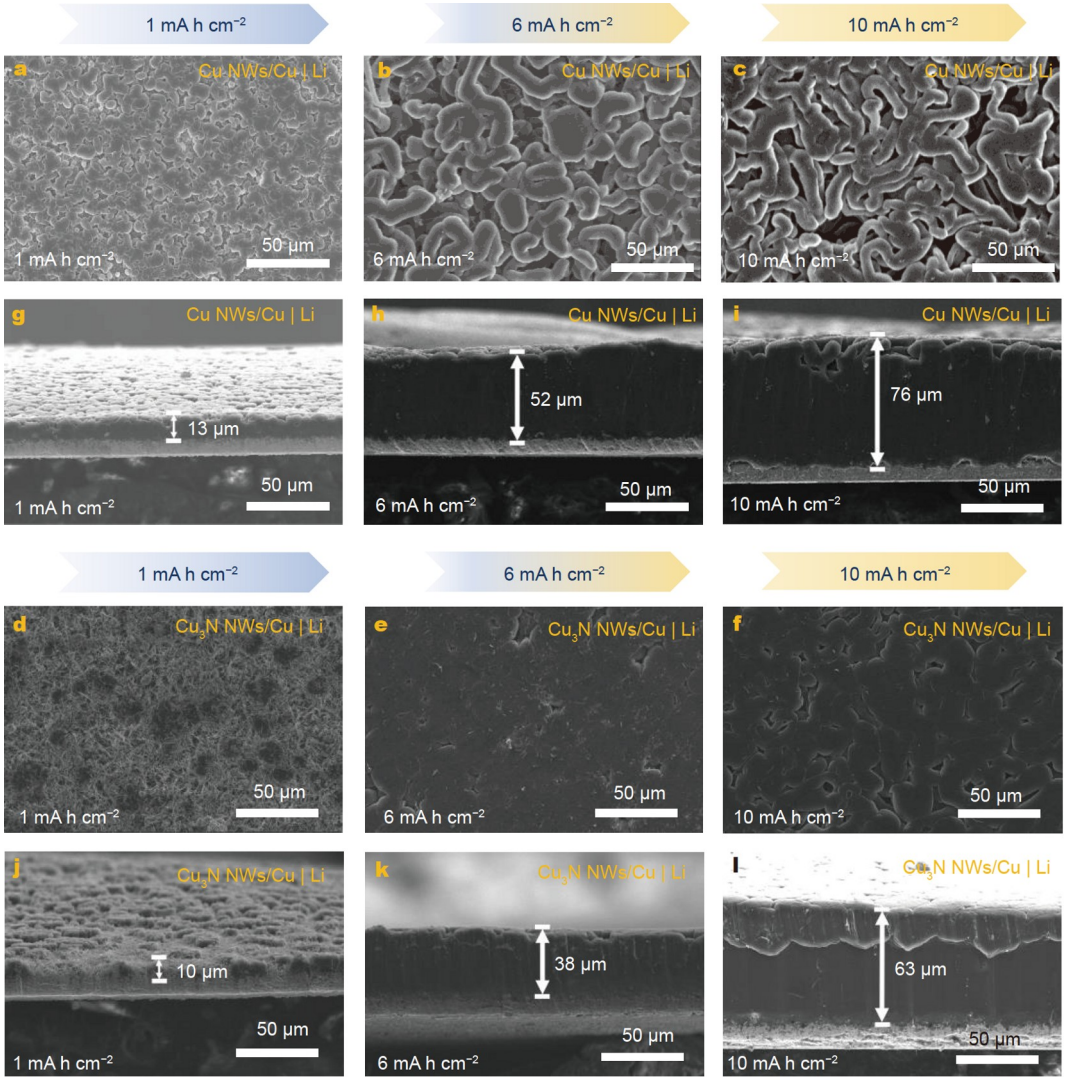

Figure 3 SEM images of Li plating on Cu NWs/Cu and Cu_3N NWs/Cu with Li content from 1 to 10 mA h cm^{-2} (1 mA cm^{-2}). Top-view SEM images of the Li morphology with 1, 6, and 10 mA h cm^{-2} Li plating on (a–c) Cu NWs/Cu and (d–f) Cu_3N NWs/Cu. Cross-sectional SEM images of (g–i) Cu NWs/Cu and (j–l) Cu_3N NWs/Cu with 1, 6, and 10 mA h cm^{-2} Li plating, respectively.

1–10 mA h cm^{-2} on different matrices. Both the homogeneity and compactness of the Li deposition improved from the Cu foil and Cu NWs/Cu to the Cu_3N NWs/Cu. On the Cu and Cu NWs/Cu matrices, Li was deposited as spheroidal particles, and the porosity was greater than that on the Cu NWs/Cu hybrid (Fig. 3 and Fig. S3). The Li deposition on the Cu_3N NWs/Cu matrix had the highest compactness and almost grew into a smooth and dense film. The differences in compactness can be clearly seen from the cross-sectional images in Fig. 3g–l and Fig. S3d–f. The thickness of the Li deposition on Cu_3N NWs/Cu was 10, 38, and 63 μm at 1, 6, and 10 mA h cm^{-2}, respectively. These thicknesses were much lower than those on the Cu NWs/Cu (13, 52, and 76 μm) and on the Cu (12, 51, and 81 μm) systems, demonstrating the dense plating of Li on the Cu_3N NWs/Cu matrix.

To confirm the reaction between Cu_3N and Li, XPS was used to investigate the surface compositions of the Cu_3N NWs/Cu and Cu NWs/Cu anodes after Li plating (Fig. 4a–c and Fig. S4). The peaks at 398.5 eV in the N 1s and 55.2 eV in the Li 1s spectra of the Cu_3N NWs/Cu–Li sample confirmed the generation of Li_3N (Fig. 4a, c). The Li_3N content in the SEI on the Cu_3N NWs/Cu–Li surface was much higher than that on the Cu NWs/Cu–Li surface. The Cu_3N NWs/Cu|Li cell showed clear voltage plateaus during the initial discharge process (Fig. S5), suggesting that the Cu_3N NWs reacted with the Li before the Li plating. In the CV curves (Fig. S6), a cathodic peak appeared at ~0.3 V *vs.* Li/Li^+ in the first cycle, which also indicated a replacement reaction from Cu_3N to Li_3N. The Li 1s and C 1s spectra (Fig. 4c and Fig. S5) showed less relative amounts of C–O and $-CO_3^{2-}$, the main decomposition products of the electrolyte, on the Cu_3N NWs/Cu matrix than on the Cu NWs/Cu matrix, indicating that the side reactions between the Li and the electrolyte were minimized. The Li_3N-rich SEI layer successfully hindered further decomposition of the electrolyte. The F 1s spectra (Fig. 4b) showed that the content of LiF in the SEI was not affected by Cu_3N.

The Li plating/stripping performances of the Cu_3N NWs/Cu and Cu NWs/Cu current collectors are shown in Fig. 5. The Cu_3N NWs/Cu|Li half-cell was stable for 260 cycles at 1 mA cm^{-2} with Li capacities of 1 mA h cm^{-2} and for 100 cycles

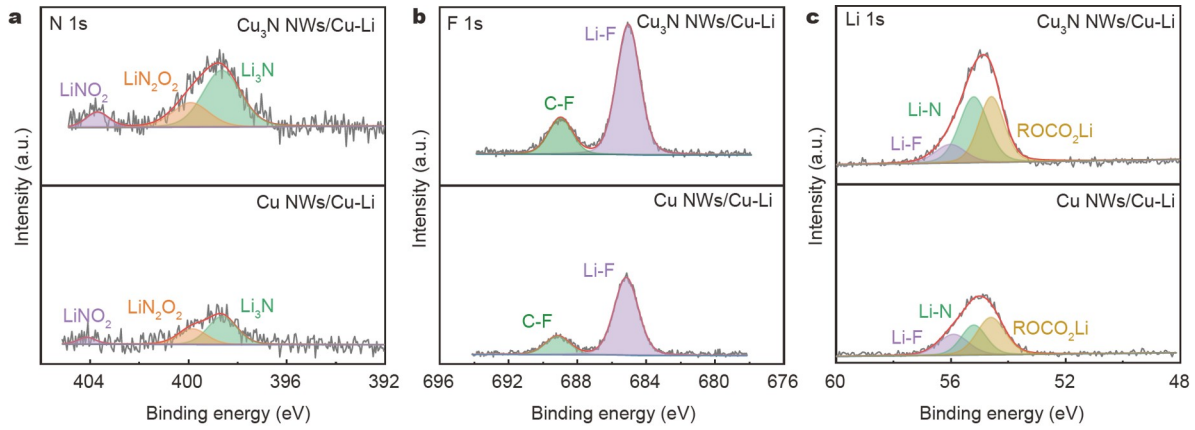

Figure 4 XPS spectra of Cu NWs/Cu and Cu_3N NWs/Cu surfaces after discharge at 1 mA cm^{-2} with 4 mA h cm^{-2} Li plating. (a) N 1s, (b) F 1s, and (c) Li 1s spectra.

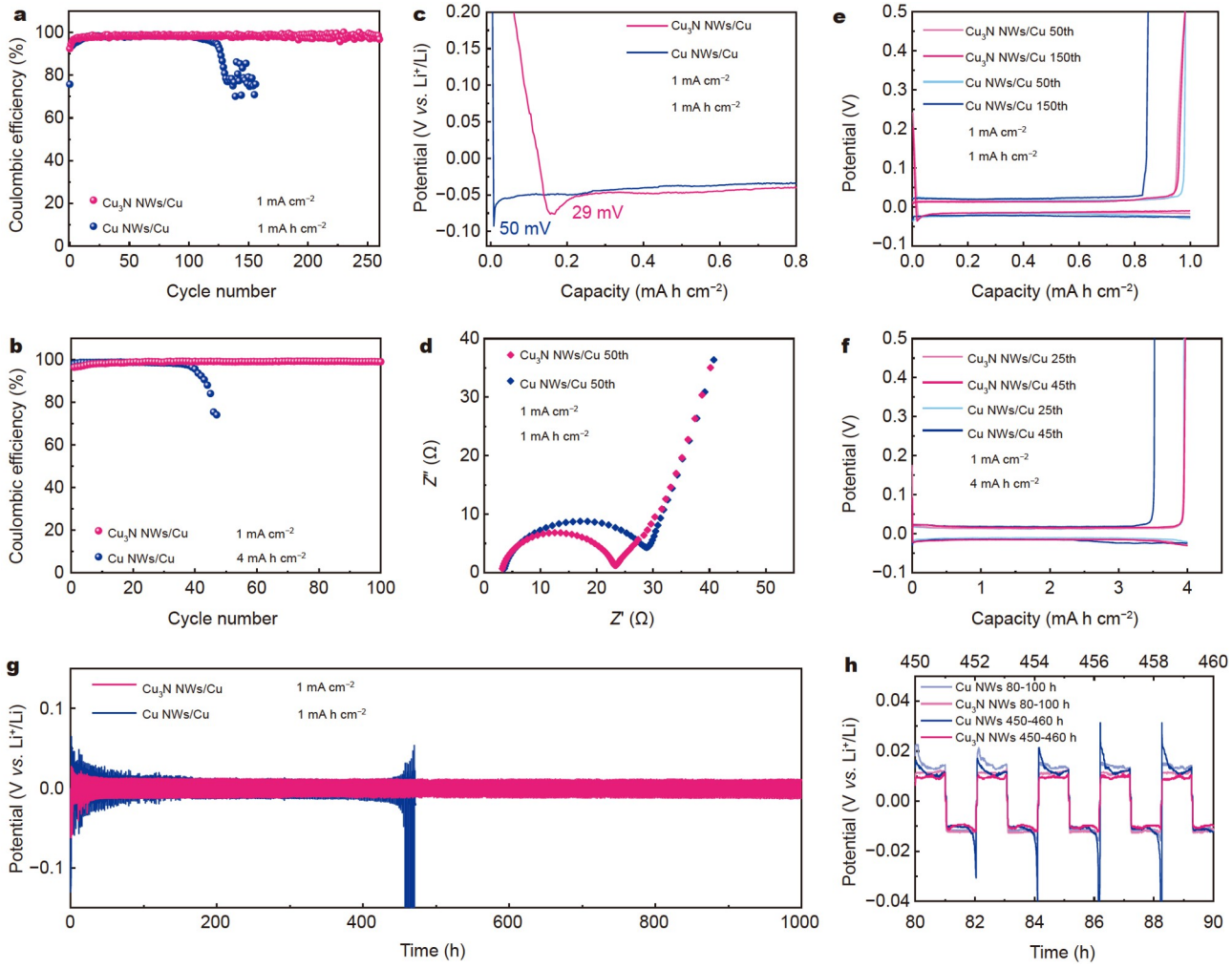

Figure 5 CE of the Cu_3N NWs/Cu|Li and Cu NWs/Cu|Li half-cell with Li capacities of (a) 1 mA h cm^{-2} and (b) 4 mA h cm^{-2}. (c) Voltage profiles for the initial Li nucleation on Cu NWs/Cu and Cu_3N NWs/Cu. (d) EIS of the Cu_3N NWs/Cu|Li and Cu NWs/Cu|Li half-cells after 50 cycles. (e, f) Charge/discharge voltage profiles of the two current collectors with 1 and 4 mA h cm^{-2} Li deposition, respectively. (g) Voltage-time profiles of the symmetric cells. (h) Magnified voltage-time profiles during the 80–90 and 450–460 h.

with Li capacities of 4 mA h cm^{-2}, respectively (Fig. 5a, b), much longer than the Cu NWs/Cu|Li half-cell (<120 and <40 cycles, respectively) and Cu|Li half-cell (<90 and <35 cycles, respectively) (Fig. S7a, b). After the initial activation, the average CE of the Cu_3N NWs/Cu|Li half-cell reached 98.9%. The plating overpotential in the initial stage of the Li deposition was the

nucleation barrier of the Li. As shown in Fig. 5c and Fig. S7c, the Cu_3N NWs/Cu–Li anode had a plating overpotential of 29 mV, much lower than that of the Cu NWs (50 mV) and the Cu foil (53 mV). EIS of the different anodes after 50 cycles are shown in Fig. 5d and Fig. S7d. Both the bulk and interface resistances of the Cu_3N NWs/Cu anode were lower than those of the Cu NWs/Cu and Cu anodes. The overpotential of the Cu_3N NWs/Cu anode was stable throughout the cycles (Fig. 5e, f). Fig. S8a–f show the surface and cross-sectional SEM images of the Cu foil, Cu NWs/Cu, and Cu_3N NWs/Cu current collectors with 4 mA h cm^{-2} Li deposition at the 10^{th} cycle. The Cu_3N NWs/Cu collector showed a dense and uniform Li plating. The lithophilic Cu_3N NWs enabled a homogeneous Li plating. The voltage-time profiles of the symmetrical cells (Fig. 5g, h, and Fig. S7e) showed that the Cu_3N NWs/Cu anode had the most stable cycle performance with a low polarization over a long cycling time of 1000 h.

To further explore the practicality of the Cu_3N NWs/Cu hybrid as a current collector in Li batteries, full cells were assembled with Li pre-deposited Cu_3N NWs/Cu, Cu NWs/Cu, and Cu foils (4 mA h cm^{-2} Li and N/P = 2.35) as anodes coupled with an LFP cathode (mass loading: 10 mg cm^{-2}). Fig. 6a and Fig. S9a show the cycling performance of the batteries at 0.5 C after activation at 0.3 C for the initial three cycles. The LFP|Cu_3N NWs/Cu–Li cell demonstrated a high reversible specific capacity of 152 mA h g^{-1} and stably cycled over 400 times with a CE as high as 99.7%, whereas the capacities of the other two batteries rapidly decayed after no more than 300 cycles. From the charge-discharge voltage profiles shown in Fig. 6b, c, and Fig. S10, the LFP|Cu_3N NWs/Cu–Li cell maintained a stable voltage profile throughout the cycles, demonstrating the structural stability of the Cu_3N NWs-LMA. Fig. 6d, e as well as Fig. S9c, d show the rate performance of the different cells from 0.3 to 5 C (1 C = 170 mA g^{-1}). The LFP|Cu_3N NWs/Cu–Li cell achieved the best rate performances of 142 and 76 mA h g^{-1} at 1 and 5 C, respectively. These performances were higher than those of the LFP|Cu NWs/Cu–Li cell (140 and 71 mA h g^{-1}) and the LFP|Cu–Li cell (139 and 65 mA h g^{-1}), indicating that Cu_3N NWs significantly improved the reversibility of the Li anode.

CONCLUSIONS

Using simple chemical processes, a commercial Cu foil was

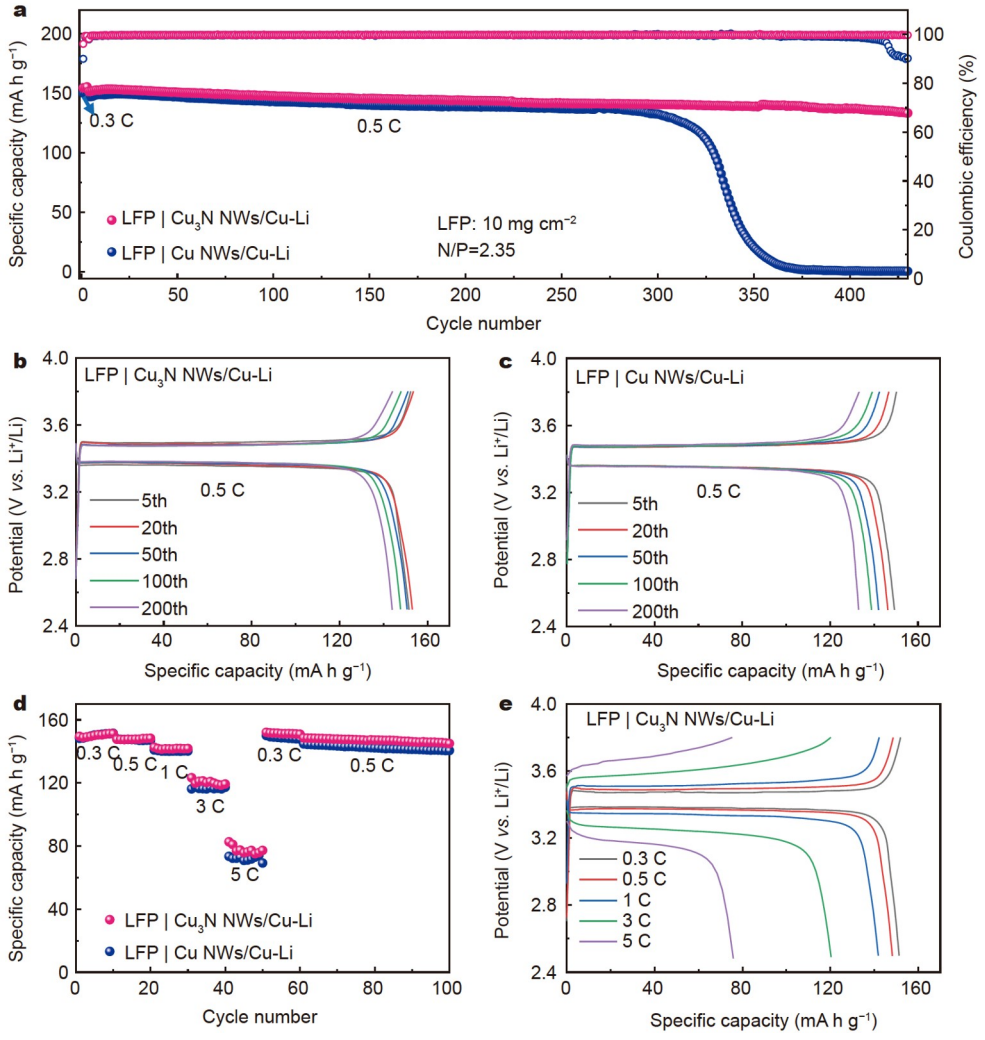

Figure 6 (a) Cycling performances of LFP|Cu NWs/Cu–Li and LFP|Cu_3N NWs/Cu–Li cells at 0.5 C. Voltage profiles of (b) the LFP|Cu_3N NWs/Cu–Li cell and (c) the LFP|Cu NWs/Cu–Li cell. (d) Rate performances of the LFP|Cu NWs/Cu–Li and LFP|Cu_3N NWs/Cu–Li cells. (e) Voltage profiles of the LFP|Cu_3N NWs/Cu–Li cell at different rates.

successfully modified *in situ* by Cu_3N NWs. During the initial Li plating process, Cu_3N was converted to Li_3N. During the repeated Li plating/stripping cycles, the lithophilic Li_3N significantly reduced the nucleation overpotential of Li, resulting in a uniform and compact Li deposition. Li_3N also contributed to the formation of a Li_3N-rich SEI that effectively minimized Li dendrite growth and prevented side reactions between Li and the electrolyte. As a result, even at a high deposition capacity of 10 mA h cm^{-2}, there was no dendrite generation. The Cu_3N NWs/Cu anode achieved a stable cycling performance with high average CEs of 98.6% for over 270 cycles at 1 mA cm^{-2} and 1 mA h cm^{-2} and 98.9% for over 100 cycles at 1 mA cm^{-2} and 4 mA h cm^{-2}. The LFP full cell with a high mass loading of 10 mg cm^{-2} achieved a stable CE of 99.7% and a significantly improved cycling stability, illustrating that the Cu_3N NWs/Cu current collector has significant potential for practical applications in Li batteries.

Received 28 December 2021; accepted 16 March 2022; published online 13 May 2022

1 Liu SF, Wang XL, Xie D, *et al.* Recent development in lithium metal anodes of liquid-state rechargeable batteries. J Alloys Compd, 2018, 730: 135–149
2 Wang Q, Liu B, Shen Y, *et al.* Confronting the challenges in lithium anodes for lithium metal batteries. Adv Sci, 2021, 8: 2101111
3 Wu H, Zhang Y, Deng Y, *et al.* A lightweight carbon nanofiber-based 3D structured matrix with high nitrogen-doping level for lithium metal anodes. Sci China Mater, 2018, 62: 87–94
4 Man J, Liu W, Zhang H, *et al.* A metal-organic framework derived electrical insulating-conductive double-layer configuration for stable lithium metal anodes. J Mater Chem A, 2021, 9: 13661–13669
5 Zhu R, Yang H, Fadillah L, *et al.* A lithiophilic carbon scroll as a Li metal host with low tortuosity design and "dead Li" self-cleaning capability. J Mater Chem A, 2021, 9: 13332–13343
6 Zhang J, Su Y, Zhang Y. Recent advances in research on anodes for safe and efficient lithium-metal batteries. Nanoscale, 2020, 12: 15528–15559
7 Ghazi ZA, Sun Z, Sun C, *et al.* Key aspects of lithium metal anodes for lithium metal batteries. Small, 2019, 15: 1900687
8 Lu W, Yang H, Chen J, *et al.* Highly elastic wrinkled structures for stable and low volume-expansion lithium-metal anodes. Sci China Mater, 2021, 64: 2675–2682
9 Guo Y, Li H, Zhai T. Reviving lithium-metal anodes for next-generation high-energy batteries. Adv Mater, 2017, 29: 1700007
10 Wang J, Liu H, Wu H, *et al.* Self-standing carbon nanotube aerogels with amorphous carbon coating as stable host for lithium anodes. Carbon, 2021, 177: 181–188
11 Zou W, Li Q, Zhu Z, *et al.* Electron cloud migration effect-induced lithiophobicity/lithiophilicity transformation for dendrite-free lithium metal anodes. Nanoscale, 2021, 13: 3027–3035
12 Jeong J, Chun J, Lim WG, *et al.* Mesoporous carbon host material for stable lithium metal anode. Nanoscale, 2020, 12: 11818–11824
13 Yu J, Shi K, Zhang S, *et al.* A lithium nucleation-diffusion-growth mechanism to govern the horizontal deposition of lithium metal anode. Sci China Mater, 2021, 64: 2409–2420
14 Zhu B, Jin Y, Hu X, *et al.* Poly(dimethylsiloxane) thin film as a stable interfacial layer for high-performance lithium-metal battery anodes. Adv Mater, 2017, 29: 1603755
15 Yang CT, Lin YX, Li B, *et al.* The bonding nature and adhesion of polyacrylic acid coating on Li-metal for Li dendrite prevention. ACS Appl Mater Interfaces, 2020, 12: 51007–51015
16 Zhang YJ, Wang W, Tang H, *et al.* An *ex-situ* nitridation route to synthesize Li_3N-modified Li anodes for lithium secondary batteries. J Power Sources, 2015, 277: 304–311
17 Li NW, Yin YX, Yang CP, *et al.* An artificial solid electrolyte interphase layer for stable lithium metal anodes. Adv Mater, 2016, 28: 1853–1858
18 Lee DJ, Lee H, Kim YJ, *et al.* Sustainable redox mediation for lithium-oxygen batteries by a composite protective layer on the lithium-metal anode. Adv Mater, 2016, 28: 857–863
19 Yan C, Yao YX, Chen X, *et al.* Lithium nitrate solvation chemistry in carbonate electrolyte sustains high-voltage lithium metal batteries. Angew Chem Int Ed, 2018, 57: 14055–14059
20 Pan H, Han KS, Vijayakumar M, *et al.* Ammonium additives to dissolve lithium sulfide through hydrogen binding for high-energy lithium-sulfur batteries. ACS Appl Mater Interfaces, 2017, 9: 4290–4295
21 Zhang Y, Qian J, Xu W, *et al.* Dendrite-free lithium deposition with self-aligned nanorod structure. Nano Lett, 2014, 14: 6889–6896
22 Jiao S, Zheng J, Li Q, *et al.* Behavior of lithium metal anodes under various capacity utilization and high current density in lithium metal batteries. Joule, 2018, 2: 110–124
23 Nie M, Demeaux J, Young BT, *et al.* Effect of vinylene carbonate and fluoroethylene carbonate on SEI formation on graphitic anodes in Li-ion batteries. J Electrochem Soc, 2015, 162: A7008–A7014
24 Jiang H, Dong Q, Bai M, *et al.* A 3D-mixed ion/electron conducting scaffold prepared by *in situ* conversion for long-life lithium metal anodes. Nanoscale, 2021, 13: 3144–3152
25 Cheng Q, Wei L, Liu Z, *et al. Operando* and three-dimensional visualization of anion depletion and lithium growth by stimulated Raman scattering microscopy. Nat Commun, 2018, 9: 2942
26 Chazalviel JN. Electrochemical aspects of the generation of ramified metallic electrodeposits. Phys Rev A, 1990, 42: 7355–7367
27 Liu Y, Gao D, Xiang H, *et al.* Research progress on copper-based current collector for lithium metal batteries. Energy Fuels, 2021, 35: 12921–12937
28 Wang R, Shi F, He X, *et al.* Three-dimensional lithiophilic Cu@Sn nanocones for dendrite-free lithium metal anodes. Sci China Mater, 2020, 64: 1087–1094
29 Huang Z, Zhang C, Lv W, *et al.* Realizing stable lithium deposition by *in situ* grown Cu_2S nanowires inside commercial Cu foam for lithium metal anodes. J Mater Chem A, 2019, 7: 727–732
30 Zhang C, Lv W, Zhou G, *et al.* Vertically aligned lithiophilic CuO nanosheets on a Cu collector to stabilize lithium deposition for lithium metal batteries. Adv Energy Mater, 2018, 8: 1703404
31 He D, Liao Y, Cheng Z, *et al.* Facile one-step vulcanization of copper foil towards stable Li metal anode. Sci China Mater, 2020, 63: 1663–1671
32 Zhang C, Lyu R, Lv W, *et al.* A lightweight 3D Cu nanowire network with phosphidation gradient as current collector for high-density nucleation and stable deposition of Lithium. Adv Mater, 2019, 31: 1970336
33 Chen K, Pathak R, Gurung A, *et al.* Flower-shaped lithium nitride as a protective layer *via* facile plasma activation for stable lithium metal anodes. Energy Storage Mater, 2019, 18: 389–396
34 Lee D, Sun S, Kwon J, *et al.* Copper nitride nanowires printed Li with stable cycling for Li metal batteries in carbonate electrolytes. Adv Mater, 2020, 32: 1905573
35 Sun C, Lin A, Li W, *et al. In situ* conversion of Cu_3P nanowires to mixed ion/electron-conducting skeleton for homogeneous lithium deposition. Adv Energy Mater, 2019, 10: 1902989

Acknowledgements This work was supported by the National Natural Science Foundation of China (22075091), the Natural Science Foundation of Hubei Province (2021CFA066), and the "Fundamental Research Funds for the Central Universities" (2021yjsCXCY026). The authors thank the technical support from the Analytical and Testing Center of Huazhong University of Science and Technology (HUST) for material characterizations and the State Key Laboratory of Materials Processing and Die & Mould Technology of HUST for SEM tests.

Author contributions Yuan L and Tang D conceived the project. Tang D designed and engineered the samples, Liao Y, Jin W, Chen J, Cheng Z, and He B helped with the characterization. Tang D wrote the paper with support from Yuan L and Huang Y. All authors contributed to the general discussion.

Conflict of interest The authors declare that they have no conflict of interest.

Supplementary information Supporting data are available in the online version of the paper.

Danlei Tang received her BS degree from Nanjing University of Aeronautics and Astronautics (NUAA), China, in 2015. She is currently a Master degree candidate at the School of Materials Science and Engineering, Huazhong University of Science and Technology. Her current research mainly focuses on lithium metal batteries.

Lixia Yuan received her BS, MS, and PhD degrees from Wuhan University. She worked as a post-doctoral researcher at Tsinghua University from 2007 to 2009. She is now a professor at Huazhong University of Science and Technology. Her research interests mainly focus on lithium rechargeable batteries.

Yunhui Huang received his BS, MS, and PhD degrees from Peking University. From 2002 to 2004, he worked as an associate professor at Fudan University. He then worked with Prof. John B. Goodenough at the University of Texas at Austin for more than three years. In 2008, he became a chair professor of materials science at Huazhong University of Science and Technology. His research group works on rechargeable batteries and electrode materials.

利用Cu_3N改性铜箔集流体提高锂金属负极的循环稳定性

唐丹雷, 袁利霞*, 廖亚祺, 靳文轩, 陈杰, 程泽晓, 李想, 何斌, 李真, 黄云辉*

摘要 在二次电池的所有固态负极中, 锂金属负极因其极高的理论比容量和极低的还原电位对促进二次电池的进一步发展具有很大的潜力. 然而, 锂负极在不断脱锂/嵌锂的过程中因锂枝晶的生长导致低库伦效率并存在安全隐患, 严重阻碍了锂金属负极的实际应用. 该研究通过化学方法在商业化的铜箔集流体表面原位修饰Cu_3N纳米线得到复合微结构型集流体(Cu_3N NWs/Cu). 引入的Cu_3N纳米线具有三维结构, 不仅可以增大集流体的比表面积、降低集流体表面的电流密度, 还可以容纳锂负极在沉积/脱嵌过程中发生的体积变化. 此外, 在首次锂沉积的过程中, Cu_3N与锂金属反应生成Li_3N($3Li + Cu_3N \rightarrow Li_3N + 3Cu$), 可以促进稳定的富含$Li_3N$的固态电解质膜(SEI)形成. 富含$Li_3N$的SEI既能增强锂离子的传输, 又能给锂的沉积提供充足的形核位点, 促进锂金属的均匀沉积, 从而抑制了锂枝晶的生长. 在锂沉积/剥离循环过程中, 这种经过Cu_3N纳米线修饰的铜箔集流体在电流密度为1 mA cm^{-2}, 锂沉积量为1 mA h cm^{-2}的条件下可以稳定循环270圈, 平均库伦效率为98.6%. 将沉积锂金属后的Cu_3N NWs/Cu–Li复合负极与$LiFePO_4$正极(正极活性物质载量: 10 mg cm^{-2}; N/P = 2.35)组装成全电池, 该全电池能稳定循环430圈. 研究表明经Cu_3N纳米线修饰的铜箔集流体在提高锂金属负极的循环稳定性方面具有良好的应用前景.